

PAPER

Quantitative imaging of carbon dimer precursor for nanomaterial synthesis in the carbon arc

To cite this article: V Vekselman *et al* 2018 *Plasma Sources Sci. Technol.* **27** 025008

View the [article online](#) for updates and enhancements.

Quantitative imaging of carbon dimer precursor for nanomaterial synthesis in the carbon arc

V Vekselman^{1,3} , A Khrabry¹ , I Kaganovich¹ , B Stratton¹ ,
R S Selinsky²  and Y Raites¹ 

¹ Princeton Plasma Physics Laboratory, Princeton, NJ 08543, United States of America

² Department of Chemical and Biological Engineering, Princeton University, Princeton, NJ 08544, United States of America

E-mail: vekselman@pppl.gov

Received 8 September 2017, revised 21 December 2017

Accepted for publication 12 January 2018

Published 6 February 2018



Abstract

Delineating the dominant processes responsible for nanomaterial synthesis in a plasma environment requires measurements of the precursor species contributing to the growth of nanostructures. We performed comprehensive measurements of spatial and temporal profiles of carbon dimers (C_2) in sub-atmospheric-pressure carbon arc by laser-induced fluorescence. Measured spatial profiles of C_2 coincide with the growth region of carbon nanotubes (Fang *et al* 2016 *Carbon* **107** 273–80) and vary depending on the arc operation mode, which is determined by the discharge current and the ablation rate of the graphite anode. The C_2 density profile exhibits large spatial and time variations due to motion of the arc core. A comparison of the experimental data with the 2D simulation results of self-consistent arc modeling shows good agreement. The model predicts well the main processes determining spatial profiles of carbon dimers (C_2).

Keywords: arc nanomaterial synthesis, laser induced fluorescence, atmospheric plasma diagnostic, arc discharge

1. Introduction

Understanding the synthesis of nanomaterials by a sub-atmospheric pressure arc discharge, such as a carbon arc for synthesis of fullerenes, nanotubes, and graphene [2–4], requires knowledge of the plasma parameters and composition in the region of nanostructure formation and growth. There is currently no satisfactory theoretical description of this process due to the lack of reliable and accurate measurements. It is challenging to perform *in situ*, non-invasive measurements in the harsh arc discharge environment. *Ex situ* evaluation of synthesized nanostructures does not provide detailed understanding of the growth mechanism and conditions. The use of probes for detection of densities, temperatures, and other environmental parameters or collection of samples has the drawback of inducing perturbations in the region of interest.

Starting from the discovery of synthesis of carbon nanotubes (CNT) in a carbon arc by Iijima [5], a variety of methods for producing carbonaceous nanostructures have been developed [6–8]. In parallel, *in situ* measurements of synthesis precursors were carried out using optical techniques. Lange *et al* [9] applied optical emission spectroscopy (OES) to study arc plasma composition and diatomic carbon (C_2) radicals; this work was continued in [10–12]. Other OES measurements of carbon species in arcs were carried out in [13, 14]. However, OES measurements are line-integrated along the observation sightline and additional assumptions are required to deduce density and temperature profiles. These assumptions introduce ambiguity in the interpretation of OES measurements. Advanced laser-based spectroscopy was applied to study carbon species in the laser vaporization synthesis method [15–17].

Carbon atoms in arc undergo several transformations before incorporating into a nanostructure. They are evaporated from the anode material in form of molecules (C_2 , C_3) [18] and larger particles [19] and then dissociated in the hot

³ Author to whom any correspondence should be addressed.

arc core to carbon atoms. At lower temperatures (3000–5000 K), carbon atoms associate back to C_2 and C_3 molecules [20], as evidenced by intense emission of molecular bands from these species. Recent studies show that the C_2 content may affect the properties of the synthesized nanomaterial [21, 22]. Abundance and the opportunity to affect the synthesis path reveal the critical role of C_2 as an important synthesis precursor.

Laser induced fluorescence (LIF) differs from other spectroscopic techniques due to its high selectivity, sensitivity and high spatial and temporal resolution. LIF is inherently free from the effects of laser background light, which is a significant advantage for application to high pressure plasmas in which scattered laser light is very intense. Sub-atmospheric pressure arc plasmas containing molecular species are characterized by complex chemistry that depends on the plasma state. The volume occupied by plasma is relatively small and features large time-evolving gradients. Thus, the LIF technique is best suited to the study of carbon precursor species participating in synthesis. A variant of LIF known as planar LIF, allows instantaneous measurement of density distribution profiles with all the benefits of conventional LIF. In planar LIF, the laser beam is shaped into a sheet geometry and a two-dimensional detector is used. LIF and planar LIF techniques are described in detail in [23–25].

Here, we report the first comprehensive measurements of spatial and temporal profiles of carbon dimers in sub-atmospheric-pressure carbon arc by the laser-induced fluorescence technique. Planar LIF was applied to obtain quantitative density distributions of C_2 in different modes of arc operation. The spatial profiles of C_2 forming a hollow spherical shape and further referred as a bubble [26] were found to coincide with growth region of CNTs [1]. Presence of C_2 and its influence on the nanotube growth in arc are currently under investigation and will be published in a separate paper. The C_2 density profiles reported in this paper are therefore of great interest for modeling of synthesis processes in the carbon arc.

1.1. Description of quantitative planar LIF

The rate equation for the population of the excited state n_2 can be written as

$$\frac{dn_2}{dt} = \frac{B_{12}}{c} n_1 I_\nu - \frac{n_2}{\tau_{\text{eff}}}, \quad (1)$$

where n_1 is the population of the lower (pumping) state, B_{12} is the Einstein absorption coefficient and τ_{eff} is the effective lifetime of the excited state which accounts for all processes leading to depopulation of the excited state. The laser stimulated depopulation term is neglected here assuming $n_1 \gg n_2$. I_ν is the spectral laser intensity defined as

$$I_\nu = \frac{E_L}{A_L \tau_L \Delta\nu_L} \Gamma, \quad (2)$$

where E_L is the laser energy per pulse and Γ is the dimensionless lineshape integral accounting for the interaction between the laser and transition absorption lineshape profiles, $\Gamma = \int a(\nu) g(\nu) d\nu$. Here, $a(\nu)$ is the absorption lineshape centered at transition frequency and normalized by unity,

$\int a(\nu) d\nu = 1$; $g(\nu)$ is the laser lineshape normalized to unity, $\int g(\nu) d\nu = 1$. A typical approximation of $\Gamma \sim 1$ reflects inequality $\Delta\nu_L \gg \Delta\nu_{\text{tr}}$ where the $\Delta\nu_{\text{tr}}$ is the transition linewidth.

The measured LIF signal S_{LIF} is proportional to the number of fluorescence photons

$$S_{\text{LIF}} = n_2 A_{21} \tau_{\text{eff}} V \frac{\Omega}{4\pi} K, \quad (3)$$

where A_{21} is the Einstein coefficient for spontaneous emission from the excited state, V is the interaction volume, Ω is the solid angle observed by the collection optics and K is a cumulative coefficient related to the properties of the detector and collection optics and the spatial profile of the laser intensity. Since the n_1 can be correlated with the population of the ground state through the Boltzmann factor, $n_1 = n_0 f_B$, the ground state density can be obtained from the measured LIF signal without accounting for saturation effect as

$$n_0 = S_{\text{LIF}} \cdot \left[f_B \frac{B_{12}}{c} \frac{E_L}{A_L \Delta\nu_L} \Gamma \cdot A_{21} \tau_{\text{eff}} V \frac{\Omega}{4\pi} K \right]^{-1}. \quad (4)$$

Direct implementation of equation (4) requires knowledge of cumulative parameter K , interaction volume and observation solid angle which are hard to obtain. Therefore, these undetermined parameters are commonly estimated by calibration via Rayleigh or Raman scattering. In appendix B, we describe in detail how these parameters were obtained by Rayleigh scattering (RS) measurements.

The phenomenon of transition saturation is important to consider in experiments with single shot LIF measurements. Balancing between signal-to-noise ratio (SNR) and linear LIF signal response shifts the level of the laser intensity towards the saturation region. In multi-shot LIF measurements the accumulation of the signal allows lowering the laser intensity keeping SNR the same. Planar LIF geometry introduces spatial dependence of the laser intensity in transverse direction (relative to the laser beam propagation); it is described in appendix B. Therefore, the saturation effect becomes, in general, space dependent; it is discussed in appendix D.

Another important phenomenon related to the LIF measurements in atmospheric plasmas is the shortening of the excited state lifetime. It is mostly due to quenching by surrounding atoms and molecules, plasma electrons and branching channels. In the synthesis arc, participation of the species of interest in synthesis processes contributes to the lifetime shortening as well. Therefore, time-resolved LIF measurement of the excited state lifetime is required (appendix C). It also allows fine tuning of the fluorescence acquisition time in planar LIF to further improve SNR.

2. Experimental setup

2.1. Arc setup

The arc system used in this experiment is an sub-atmospheric pressure DC arc discharge that is described in detail in [26]. It

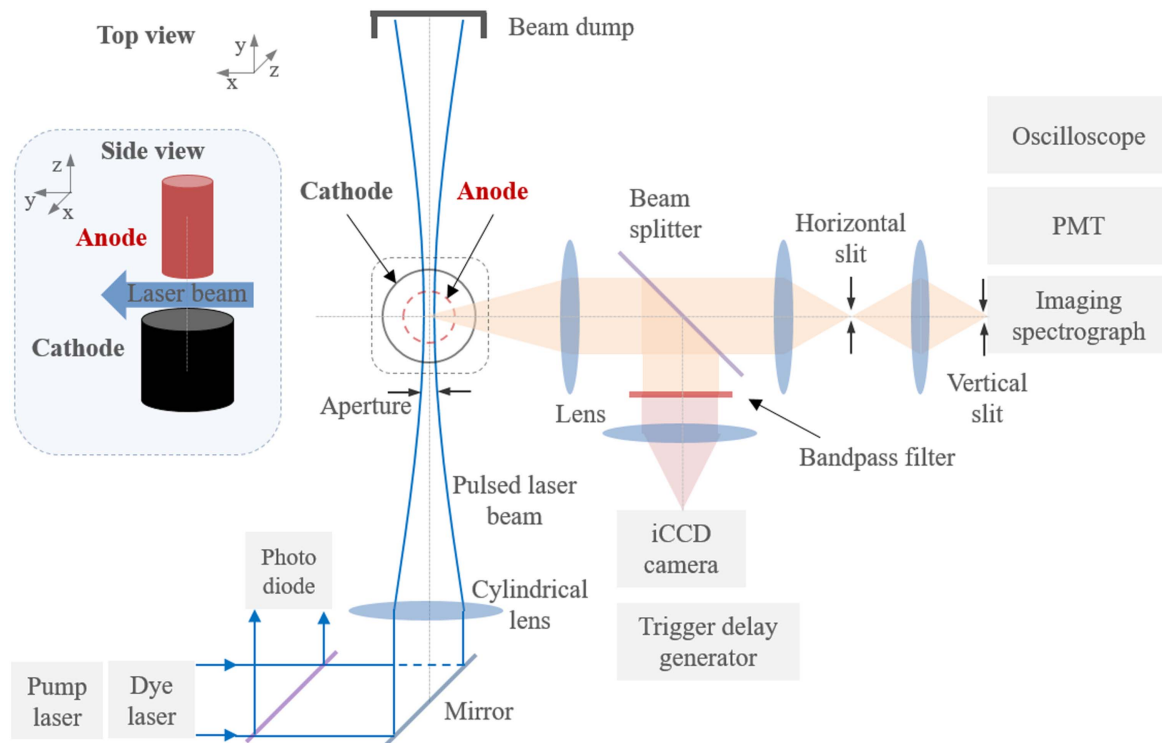


Figure 1. Schematic of the experimental setup and LIF diagnostics.

consists of a stainless steel 6-way cross equipped with four optical viewports allowing access to the inter-electrode region where the plasma is formed. Two graphite electrodes of 9.5 mm (cathode) and 6.5 mm (anode) in diameter are aligned vertically and their position can be adjusted via two computer controlled motorized translational stages. Helium was used as the buffer gas. The flow of helium was regulated by a feedback controlled vacuum line and flow needle valve via a PID algorithm (using LabVIEW) to maintain 66.7 kPa total pressure in the chamber. The arc setup and LIF diagnostic assembly are schematically shown in figure 1.

The arc between graphite electrodes was initiated by bringing the electrodes into contact and then moving them apart. The power supply maintained a constant discharge current while the discharge voltage was determined by the inter-electrode gap length. There are two modes of arc operation that differ by the anode ablation rate [26]. In the low ablation mode, the anode material ablation rate is below 1 mg s^{-1} and almost independent of the arc current. In contrast, the high ablation mode features larger anode ablation rates (up to 10 mg s^{-1}) and strong correlation with the current. A recent study has also revealed dependence of the ablation rate on the gap length at fixed current. The transition between low and high ablation mode occurred at about 55 A current for a given electrode geometry.

The two arc operation modes are also characterized by different arc behavior. Arc core motion is confined between the electrodes in the low ablation mode and oscillates with frequencies up to 10 kHz. In high ablation mode, the arc core attachment extends to the side surface of the anode and features additional oscillations that are dominant in the

frequency range below kHz [27]. Such unpredictable dynamics of the arc complicates the application of the diagnostics. This difficulty was overcome by implementing LIF diagnostic in planar geometry described in next section. It allows us to obtain spatial density profiles of C_2 in a single measurement within tens ns time thus effectively eliminating effects of arc motion. In the current paper, we present results for discharge currents of 50 and 60 A corresponding to the low and high ablation modes of the carbon arc.

2.2. Planar LIF setup

The planar LIF diagnostic setup was employed to obtain instantaneous density distribution profiles. The LIF laser system consisted of a Spectra-Physics (Sirah) Cobra-Stretch dye laser pumped by the third harmonic (355 nm) of a Continuum SL-III Nd:YAG laser. For excitation of the C_2 (3, 1) transition used in this study, Coumarin 440 laser dye dissolved in ethanol was used. The dye laser was operated near 437 nm with a linewidth of 0.06 cm^{-1} . The fluorescence was detected near 470 nm. The output energy of the pump laser was approximately 100 mJ and the dye laser output energy was about 10 mJ, with an estimated energy fluctuation of 12%. The dye laser beam passed through a variable attenuator (1/2 wave-plate and linear polarizer mounted on a rotational stage), which allowed the laser energy to be varied continuously. The laser beam was then directed into an adjustable aperture installed in front of the chamber entrance quartz window.

Planar LIF utilizes a sheet-like laser beam profile oriented vertically along the axis of the arc electrodes. The beam shaping was achieved by a cylindrical lens as shown in

figure 1. The thickness of the laser beam was estimated to be $50\text{ }\mu\text{m}$ using the Rayleigh criterion. The height of the laser beam was limited by the aperture. Due to the laser shaping, the transverse profile of the laser beam intensity shows a gradual decrease toward the edges (see appendix B). This implies a need for a laser power distribution correction for the LIF measurements in planar geometry.

An intensified CCD (iCCD, Andor iStar) camera was used to obtain the LIF signal from the sheet-like interaction volume in one laser shot. The iCCD camera was coupled to an objective lens and bandpass filter (Andover 470FS10-50, centered at 470 nm with bandwidth 10 nm). The spatial resolution was $1/36\text{ mm}$ per pixel. The exposure time of the iCCD camera was adjusted to match the duration of the fluorescence signal (see appendix C) to minimize the collection of radiation from the plasma volume passing through the bandpass filter. The background was subtracted from the collected signal. However, this subtraction is a key contributor to the measurement error due to the long time intervals between subsequent acquisitions with the laser on and off.

3. Results and discussions

Measurements of C_2 spatial density profiles were conducted in low and high ablation mode of the arc operation [28]. Comprehensive analysis of the nanomaterials synthesized in the arc operated in high ablation mode can be found elsewhere [29, 30]; however, to the best of our knowledge, there are no reports of nanotube synthesis in the low ablation mode. We carried out *ex situ* evaluation of the nanomaterials produced in the low ablation mode by transmission electron microscopy (TEM) and Raman spectroscopy. While both modes were confirmed to produce single-walled carbon nanotubes (SWCNTs), single-walled carbon nanohorns (SWCNHs), and amorphous carbon, the ratio of SWCNTs to other carbon nanomaterials, is higher for samples collected in high ablation mode than low ablation mode (see appendix F for details of nanomaterial evaluation). These results confirm that the plasma species observed and the nanostructures synthesized are correlated.

3.1. Experimental results

A set of frames showing the measured C_2 density distribution during the first half minute of the arc operated at 50 A current is shown in figure 2. This current corresponds to the low ablation mode of the arc. The arc voltage and current waveforms are shown in the bottom-left with time markers corresponding to recorded planar LIF images (1)–(4). After initiation of the arc, C_2 always dominates in the region near the anode surface ablated by the arc core (figure 2). However, flare-like structures of C_2 extending towards the cathode can be observed during the first several seconds as seen in figures 2(1) and (3). Typical C_2 densities in these flares are in the range 10^{16} – 10^{17} cm^{-3} . At these times, the C_2 distribution is non-uniform and asymmetric relative to the

electrode axis. It is unclear if C_2 is formed in the anode vicinity due to evaporation from micro-particles [19] and large molecules dissociation [18] or from the carbon atom flux from the evaporated anode.

Later in time, corresponding to images (3) and (4), the bubble-like structure of the C_2 distribution is formed and remains until the arc extinction. LIF images shown in figure 2 are selected arbitrary and were generated from the intersection of the laser sheet beam with C_2 volumetric distribution and therefore the observable shape of the bubble is affected by the bubble position. While the distribution of C_2 shown in figure 2(4) is mostly observed in the low ablation mode, these images show that plasma species distribution evolving in time and space should be known during the material collection and probing.

In this regime, the largest density of C_2 up to $3 \times 10^{16}\text{ cm}^{-3}$ is observed near the anode surface. In the bubble boundary layer, the density is in the 10^{15} cm^{-3} range. The size of the C_2 bubble in the radial direction is larger for larger gaps l_{gap} and typically exceeds the anode size when $l_{\text{gap}} \geq r_a$, where r_a is the anode radius.

At small gaps ($l_{\text{gap}} < r_a$), the C_2 bubble is confined between electrodes and exhibits sporadic motion, see figure 3. As was shown by the fast frame imaging diagnostic in [26], the bubble follows the arc core dynamics. In figure 3, the arc is operated in high ablation mode and C_2 densities in the bubble boundary layer are approaching few 10^{16} cm^{-3} . The C_2 density near the anode surface is up to 10^{17} cm^{-3} . The C_2 concentration increase is mainly due to the increase of the current and partially due to the decrease of the gap length.

The size of the C_2 bubble is smaller for shorter gaps as it is clearly seen by comparing figures 2(4) and figure 3(2). However, in both cases of small and large gaps, the bubble boundary extends up to a distance of 3–5 mm in the radial direction (compare figure 2(4) and figure 3(3) or figure 3(1)). In the high ablation mode, the presence of C_2 at 5 mm radial distance is due to the bubble motion (e.g. the bubble shifts off the electrode axes). This is an important observation because recently applied fast movable witness plate diagnostics detected CNTs at radial distances 3–11 mm [1]. Thus, from the synthesis point of view, C_2 can be present in the growth region following two different scenarios corresponding to low and high ablation modes:

1. With concentration about 10^{15} cm^{-3} and small variation during the arc operation (low ablation mode)
2. With concentration above 10^{16} cm^{-3} but time-dependent, determined by the bubble (arc) motion (high ablation mode).

The highest yield of synthesis of carbon nanomaterials (e.g. nanotubes) is typically obtained in arcs operated in high ablation mode with short inter-electrode gaps. This is well correlated with observation of the largest concentration of the carbon molecular precursor (C_2) in this regime. Therefore, the C_2 density values and time evolution in synthesis region are important inputs for synthesis modeling. It follows from the arc modeling described in the next section that the C_2 content is high in the synthesis

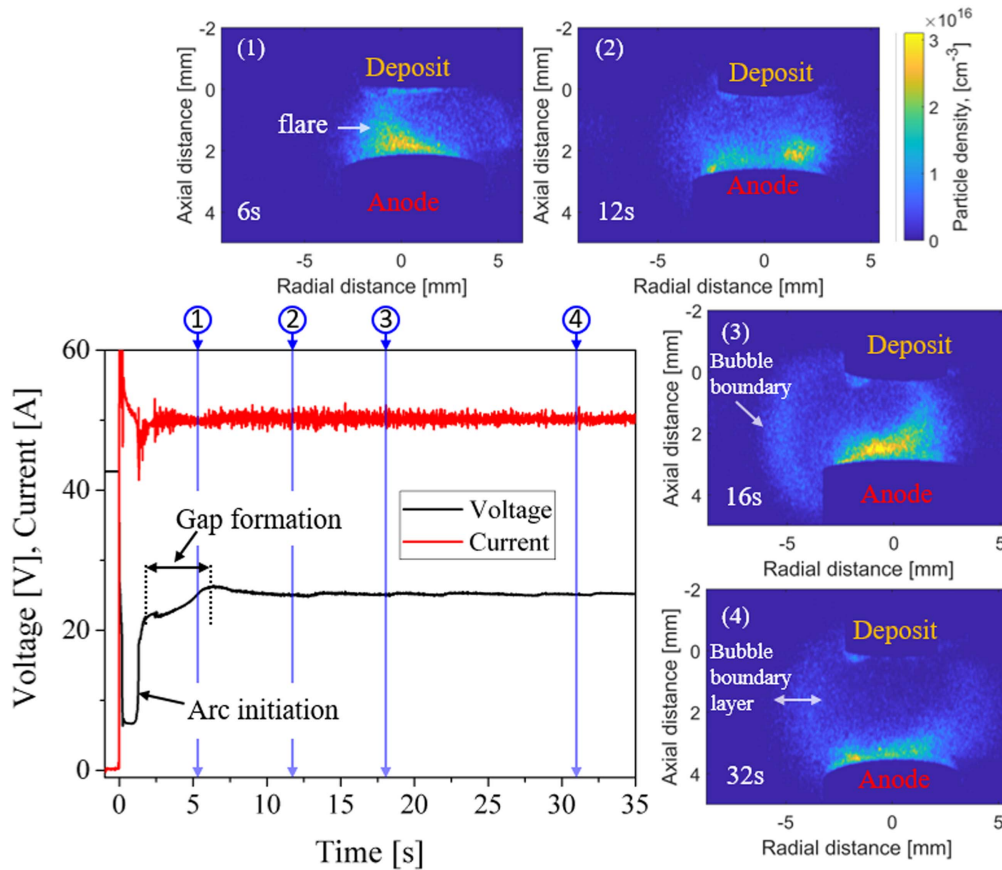


Figure 2. Evolution of the C_2 density distribution in arc in low ablation mode (current 50 A). Time is increasing from (1)–(4) and shown in the bottom-left corner. Final inter-electrode gap length is about 3 mm. Anode 6.5 mm in diameter, cathode—9.5 mm.

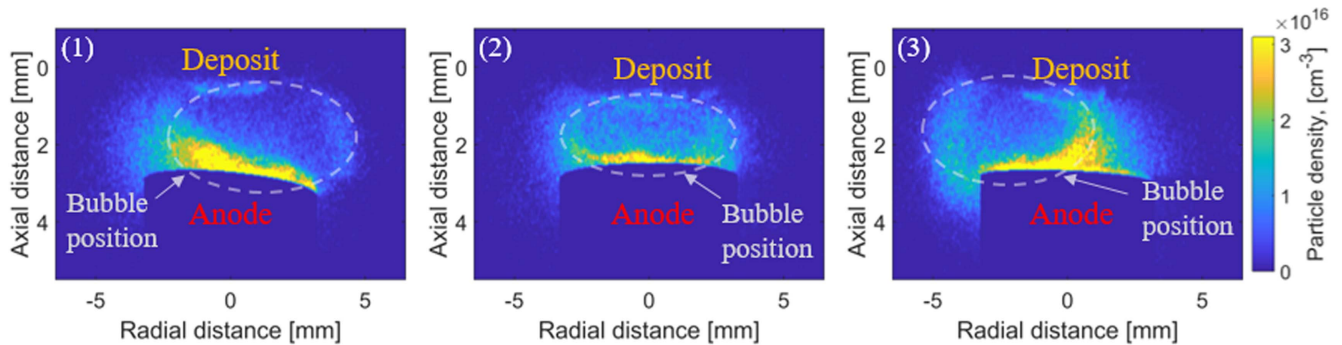


Figure 3. The C_2 density distribution in arc discharge in high ablation mode (current 60 A) showing the bubble motion. Frames are selected arbitrary during the arc run. Inter-electrode gap length is about 2 mm. Anode 6.5 mm in diameter, cathode—9.5 mm.

region (temperature 2000–4000 K) where catalyst particles condense into droplets and CNTs grow.

3.2. Modeling

The measurements presented in this work are complemented by 2D-axisymmetric simulations of carbon arc discharge in helium atmosphere and by analytical relations allowing simple estimation of C_2 molecules number density in the C_2 maximum concentration region (the C_2 bubble layer).

3.2.1. Comparison with results of 2D simulations. The 2D steady state simulations of carbon arc discharge in helium

atmosphere performed with the computational fluid dynamics code ANSYS CFX which was customized for this purpose. A fluid model of the plasma was coupled with models of heat transfer and current flow in the electrodes to allow self-consistent determination of temperature and current density profiles, non-uniform ablation, and deposition of carbon at surfaces of the electrodes. The ratio of carbon to helium concentrations in the gas mixture was determined via solving a diffusive transport equation for ‘general’ carbon; a chemical composition of carbon species was assumed to be in a local equilibrium and was calculated using Gibbs energy minimization approach like one used in [20]. Non-equilibrium effects in the plasma, such as thermal and

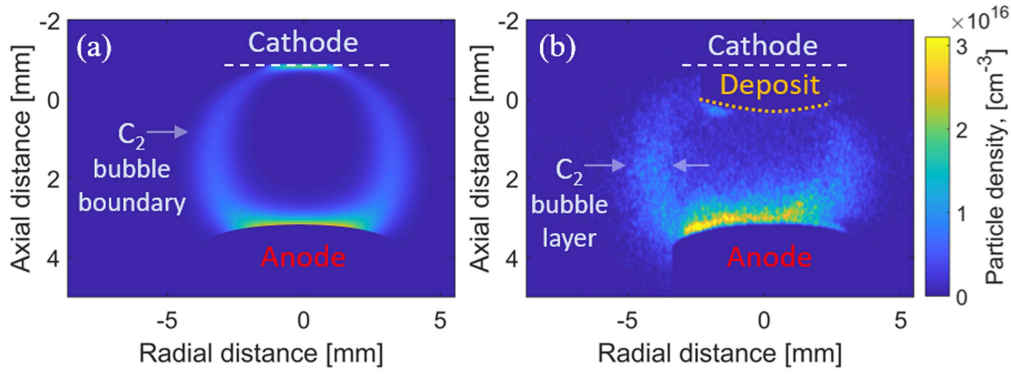


Figure 4. Comparison of (a) simulated and (b) measured C_2 density distribution in the arc at current 50 A. change in the cathode surface topology due to the growth of deposit (b) was not accounted for in the simulation (a).

ionization non-equilibrium, electron diffusion, thermal diffusion and charge separation in near-electrode sheathes were accounted for more accurate description of the plasma–electrode interaction. This enables better prediction of ablation and deposition areas and temperature profiles to determine the distribution of carbon species in the plasma volume. Transport coefficients in plasma were taken from [31]. The plasma model was benchmarked [32] against previous numerical studies [31]. Detailed description of the 2D simulations and produced results will be published in a separate paper.

The result of a 2D simulation showing the density distribution of C_2 in the arc is presented in figure 4(a). The input parameters for the model are the same as in the experiment described in the preceding sections of this paper (graphite electrodes, 6.5 mm anode and 9.5 mm cathode in diameter, 66.7 kPa helium gas pressure, current 50 A). However, while the carbon fluxes towards the cathode were accounted for in the model, the geometry change due to the growth of the cathode deposit was not simulated, i.e. the cathode surface remains flat in the simulation in contrast to deposit formation in experiment, as shown in figure 4. The obtained C_2 density distribution shown in figure 4(a) features the bubble-like shape similar to the shape seen in the measurements shown in figure 4(b). The bubble size, bubble boundary layer thickness and density obtained from the simulation are in good agreement with the experiment. In addition, the simulation showed extensive formation of C_2 near the anode surface as observed in the experiment.

3.2.2. Analytical solution for C_2 density in the bubble layer.

The density of C_2 molecules in the bubble boundary layer can also be estimated analytically from the transport equation for carbon atoms. According to the simulations and measurements, carbon is present only in atomic form in the arc core, where temperature is about 10 000 K [26]. Approaching the arc periphery, the temperature decreases and reaches a range at which C_2 molecules are significant fraction of the composition of the carbon species mixture; this region corresponds to the bubble boundary layer further denoted as the bubble layer, see figure 4 for notation. According to the mixture composition calculations in

appendix E, this temperature range is about 4000–5000 K; at lower temperatures, larger carbon molecules are the primary species present. According to this general picture, carbon atoms diffuse from the arc core through the bubble layer where they associate and form carbon molecules. Note that according to the simulations, in the bubble layer, helium atoms are the dominant species, because this region is sufficiently far from the anode ablation area. The total flux of carbon atoms through the entire bubble can be estimated as:

$$\Gamma_{C,out} = 2\pi R_{bubble} d_{arc} \cdot D_{C-He} \frac{n_{C,in}}{L_{bubble}}, \quad (5)$$

where R_{bubble} is the radius of the bubble, d_{arc} is the inter-electrode gap, L_{bubble} —thickness of the bubble layer, $n_{C,in}$ is the carbon density at the inner side of the bubble boundary, D_{C-He} is the diffusion coefficient of carbon in helium, which can be expressed as:

$$D_{C-He} \approx \frac{1}{3} \frac{v_{th,C}}{n_{He} \sigma_{C-He}}. \quad (6)$$

Here, $\sigma_{C-He} \approx 3 \times 10^{-19} \text{ m}^2$ [33] is collisional cross-section, n_{He} is helium number density, $v_{th,C}$ is thermal velocity of carbon atoms:

$$v_{th,C} = \sqrt{\frac{8kT}{\pi m_C}}, \quad (7)$$

where k is the Boltzmann constant, T is the gas temperature in the bubble layer, and m_C is the carbon atom mass. The helium number density can be assessed from:

$$n_{He} \approx \frac{p}{kT}, \quad (8)$$

where p is the total background gas pressure.

The total flux of carbon atoms escaping from the arc core can be also determined from the difference between measured rates of carbon ablation from the anode surface and its deposition on the cathode $\Gamma_{C,out}$, which is about 0.2 mg s^{-1} [26]

$$\Gamma_{C,out} = (G_{ablation} - G_{deposition})/m_C. \quad (9)$$

Knowledge of the carbon flux escaping from the arc allows us to estimate the carbon density at inner side of the

bubble boundary, $n_{C,in}$, from equation (5) and then express number density of C_2 molecules. According to our estimations, density of C_2 molecules is roughly equal to $1/4$ of C atoms density in the temperature range corresponding to high concentration of C_2 molecules (see appendix E). Thus, the average density of C atoms is:

$$n_{C_2,bubble} \approx \frac{1}{4}n_C \approx \frac{1}{8}n_{C,in}. \quad (10)$$

Note that ratio R_{bubble} to L_{bubble} in equation (5) is defined by radial temperature profile in the arc, which is rather similar in most carbon arcs and is about 3.

Finally, from equations (5)–(10) it follows that:

$$n_{C_2,bubble} \approx \frac{G_{ablation} - G_{deposition}}{48\pi m_C D_{C-He} d_{arc}}. \quad (11)$$

For the arc with inter-electrode gap length of 4 mm, equation (11) predicts C_2 density is about $8 \times 10^{15} \text{ cm}^{-3}$, which is within the range of simulated and measured results.

4. Implications for understanding the synthesis processes

The results of this study have several important implications for understanding the synthesis of nanomaterials in a carbon arc:

- The C_2 bubble boundary layer is located in the reported single-wall CNT growth region. According to our simulations and [20], the formation of C_2 is followed by the formation of larger carbon molecules, C_3 , C_4 , etc. The recent study [22] shows that presence of the C_2 can accelerate nucleation processes in a CVD synthesis of CNTs. Therefore, molecular carbon plays an important role in the synthesis process and should be considered in synthesis simulations.
- The dynamics of the C_2 bubble, mostly populated in the boundary layer, introduce an additional time dependence in the synthesis path. Synthesis in carbon arcs, routinely operated in high ablation mode, is modulated due to the arc dynamics that has not been considered in synthesis simulations. Although the intrinsic time scale of nanostructure growth is believed much shorter than the μs time scale of the arc oscillations, it can affect the properties of the synthesized nanomaterial due to non-intentional functionalization in such a time varying plasma environment. This follows from comparison of the ms-time scale of the nanostructure movement through the bubble layer and the tens of μs characteristic arc oscillation time.

5. Conclusions

Quantitative measurement of the spatial profiles of dominant precursor species participating in nanomaterial synthesis is critical for understanding the processes leading to growth of nanostructures such as CNTs in the carbon arc plasma. We presented the results of a quantitative study of carbon dimer (C_2) spatial profiles by the planar laser induced fluorescence (LIF) technique. This technique is applied for the first time to a carbon arc for nanomaterial synthesis at sub-atmospheric pressure. The results not only confirm the recently observed [26, 27] bubble-like structure of C_2 in the carbon arc which coincides with the growth region of CNTs [1], but also provides absolute values for the densities of molecular carbon species.

The highest C_2 density is observed near the surface of the graphite anode consumed by the arc evaporation, 10^{16} – 10^{17} cm^{-3} . In the volume of the inter-electrode gap, the C_2 spatial profile has a distinguished bubble-like shape with densities in the range of 10^{15} – 10^{16} cm^{-3} . This shape is formed shortly after the arc initiation and strongly affected by the length of the inter-electrode gap. The measured profiles of C_2 densities are in good agreement with simulation results.

It was found that different conditions form in the growth region of nanostructures for two arc ablation modes. In the high ablation mode, the C_2 concentration is in 10^{16} cm^{-3} range, but the bubble-like spatial profile undergoes a sporadic motion following the arc core dynamics. In contrast, in arcs operated in the low ablation mode, the C_2 concentration in the bubble boundary layer is low, in the 10^{15} cm^{-3} range, and the bubble does not move largely during the arc duration. However, in both arc modes the location of the C_2 bubble layer (3–5 mm from the electrode center) coincides with reported region of CNT growth [1]. The results of this study are important for further development of predictive models of nanomaterial synthesis in carbon arcs.

Acknowledgments

The authors are grateful to A Merzhovsky and T Huang for support with assembly and calibration of the experimental setup, and to Dr Bruce Koel (Princeton University), Dr M Shneider (Princeton University), Dr A Gerakis (PPPL), Dr S Yatom (PPPL), Dr V Nemchinsky and Dr A Khodak (PPPL) for fruitful discussions.

The arc experiments, modeling and LIF measurements were supported by the US Department of Energy, Office of Science, Fusion Energy Sciences under contract No DE-AC02-09CH11466. The development of LIF setup and materials evaluation conducted in this work were supported by the US Department of Energy (DOE), Office of Science, Basic Energy Sciences, Materials Sciences and Engineering Division.

The digital data for this paper can be found at <http://arks.princeton.edu/ark:/88435/dsp01x920g025r>.

Appendix

This appendix describes the steps carried out to calibrate the LIF setup and to process planar LIF images to obtaining quantitative measurements of the C_2 density in the arc discharge. It includes a description of LIF tuning to the (3, 1) transition, RS measurements to obtain calibration constants of the LIF detection system, evaluation of the saturation effect, and determination of the effective lifetime of the excited state.

Appendix A. LIF tuning

Two procedures in the calibration of the planar LIF setup were carried out using a conventional LIF setup. First, we describe the tuning of the LIF laser to the C_2 (3, 1) transition wavelength. In conventional LIF measurements the fluorescence radiation from the interaction volume was imaged by an $f/4$ optical system onto the entrance slit of a spectrometer (Horiba iHR550 with 2400 gr mm^{-1} grating). The light-collection system optical axis was perpendicular to the laser beam. The image formed by the collection lens was spatially filtered using two adjustable slits, defining the probed interaction volume as the intersection of the laser beam and observation cone as shown in figure 1. The photo-multiplier tube (PMT, Hamamatsu R1894) was coupled to the output of the spectrometer, which was equipped with an additional motorized slit to control the spectral bandwidth of the light entering the detector. As a result, undesired light (stray light, scattered radiation from optical elements, laser beam and especially plasma emission) were effectively suppressed by a 0.4 nm spectral window.

The pump laser was controlled by a trigger generator (BNC 575). Signals from the PMT and the photodiode were recorded by a 1 GHz oscilloscope (Lecroy WaveSurfer 10). To ensure reliable detection of the LIF signal the oscilloscope was triggered by a reference TTL signal generated by the trigger generator, accounting for the time delay of the laser beam output (Q-switch and delays in internal electrical circuits) and propagation time. This approach also ensures the background signal recording during desired time interval.

The laser beam was expanded along a distance of 2 m to form a uniform beam profile at the aperture plane. This served to diminish the possibility of local saturation by laser spots ruining the LIF measurements. During the LIF measurements the laser beam energy was kept below $50 \mu\text{J}$. Laser energies were monitored using a photodiode that was calibrated by an energy meter (Thorlabs PM121D) with a pyroelectric head (Thorlabs ES220C).

As reported in a previous work [26], the Swan bands ($a^3\Pi_u - d^3\Pi_g$) of C_2 are major contributors to the arc emission in the visible wavelength range. The Swan (3–1) band was used for measurements of C_2 density distribution in this work.

Figure A1 shows a LIF excitation scan around the (3, 1) bandhead.

The band structure was not observed due to the limited duration of the arc operation and the time- and space-

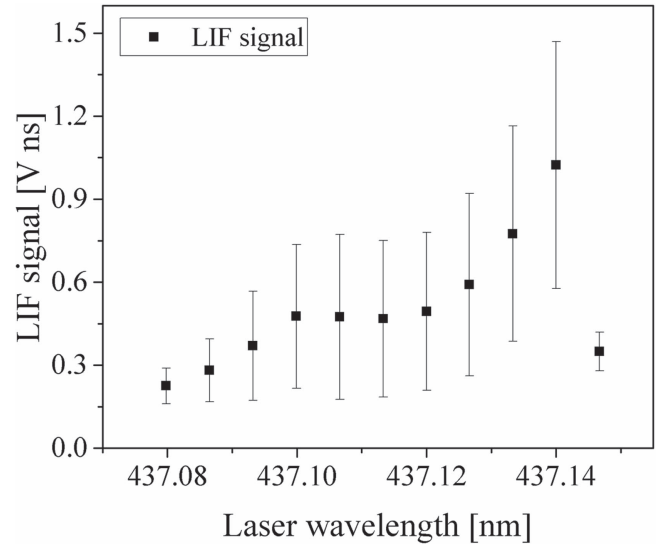


Figure A1. Laser wavelength scan near the (3, 1) bandhead of the C_2 Swan band. The fluorescence is collected near 469 nm . The arc discharge current was 55 A .

variation of the C_2 distribution in the arc. The region of C_2 formation, which partially correlates with the emission pattern and has a bubble-like shape, evolves in space (mm scale) and time (kHz range) due to motion of the arc core [26]. Therefore, the probe volume, which is fixed in space, contains carbon dimers in different states for each subsequent laser shot, which are separated by a 0.1 s interval. This difficulty can be partially overcome by cross-correlation of the C_2 bubble position with the laser shots and by operating the arc in low ablation mode. In this regime, the C_2 bubble fluctuations are strongly suppressed and behave like so-called breathing oscillations where the bubble center of mass remains fixed in space. Together with statistical averaging of the LIF signals the obtained excitation spectrum was only used for the tuning of the laser wavelength to the (3, 1) transition. The C_2 absolute density measurements were carried out using planar LIF.

Appendix B. Rayleigh calibration

The planar LIF diagnostic was calibrated by RS in air. The main objectives of this calibration were:

- To obtain the energy distribution profile of the sheet laser beam; and
- To obtain all the terms depending on the probe volume, parameters of optical elements used in signal acquisition and the detector efficiency, etc, required in equation (4) to obtain quantitative planar LIF measurements.

In the RS calibration of the planar LIF system, the alignment of the beam, laser energy per pulse, voltage applied to the photo-multiplier tube, and ICCD camera settings were kept identical to those used for the LIF measurements in the

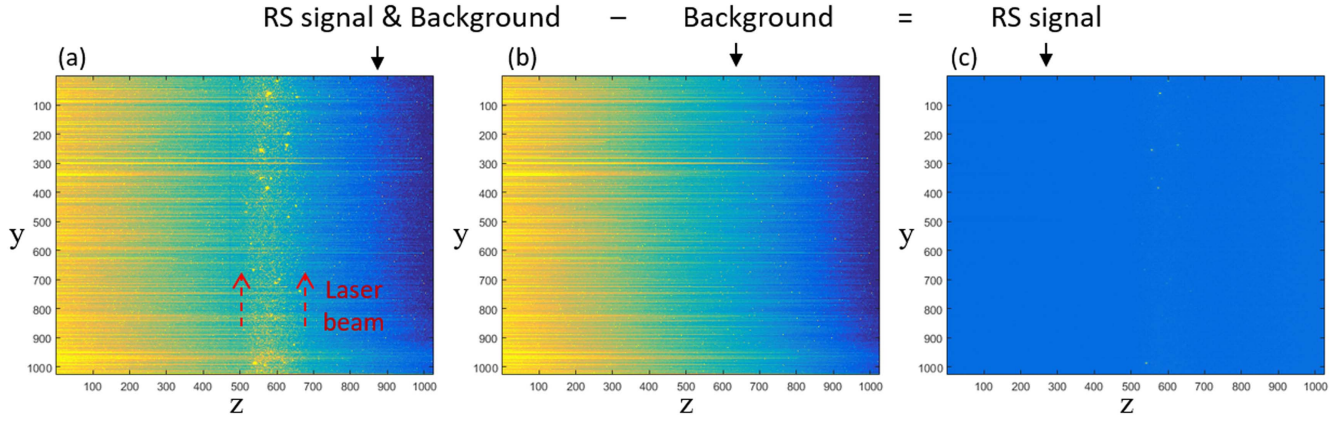


Figure B1. Example of recorded raw image of the RS signal in air with background (a), recorded background (b) and the RS signal (c) resulting from subtraction of (b) from (a).

arc. Since the RS process is less efficient than resonance photon absorption, the RS signals were small and a number of RS images were accumulated to achieve the desired SNR. The background was then subtracted to obtain a 2D distribution of the RS signal as schematically shown in figure B1. The bright spots seen in figures B1(a) and (c) and originated from impurities in the air were removed in post-processing.

The RS signal distribution in the transverse direction of the sheet laser beam was obtained by summing the camera pixel intensities along the beam propagation direction (vertical direction in figure B1) as shown in figure B2. Since the RS signal is proportional to laser energy, $S_{RS} \propto E_L$, the obtained distribution was used to calculate the normalized laser beam energy distribution profile in the transverse direction (z) as

$$\rho_L(z) = \frac{\sum_y S_{RS}(y, z)}{\sum_{y,z} S_{RS}(y, z)}, \quad (12)$$

where y and z are the coordinates of the individual pixels. Thus, the actual laser energy distribution in the RS measurements can be calculated as $E_L^{RS}(z) = \rho_L(z) \bar{E}_L^{RS}$ with \bar{E}_L^{RS} being the total laser energy per pulse measured by a pyroelectric detector.

The close proximity of the LIF excitation and fluorescence wavelengths allows the same profile to be used for LIF signal measurements:

$$E_L^{LIF}(z) = \rho_L(z) \bar{E}_L^{LIF}. \quad (13)$$

The RS signal is also proportional to the laser fluence, $I_L = \frac{E_L^{RS}}{A_L}$, where \bar{E}_L^{RS} is the laser energy per pulse and A_L is the laser beam cross-sectional area. It can be expressed similarly to equation (3):

$$S_{RS} = n_{gas} V \frac{\lambda_L}{hc} \frac{d\sigma_{RS}}{d\Omega} \Omega K I_L. \quad (14)$$

Here, V is the interaction volume, n_{gas} is the particle density of the scatterers, Ω is the light collection solid angle, K is the cumulative constant including response function and efficiency of the acquisition system. The RS cross-section,

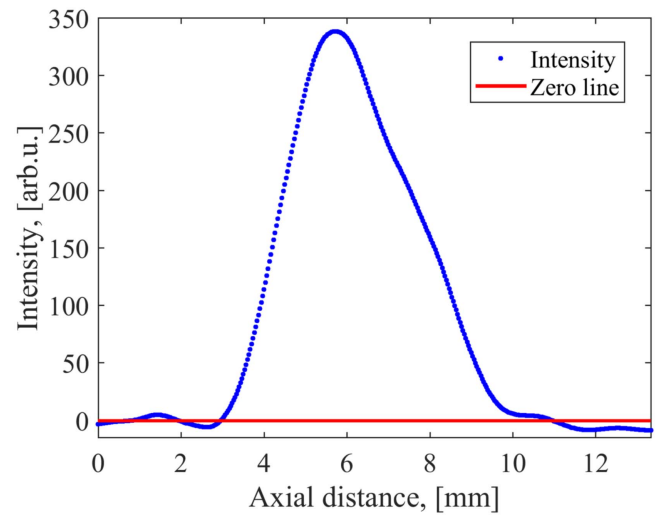


Figure B2. Transverse energy distribution within the planar LIF laser beam.

$4\pi \frac{d\sigma_{RS}}{d\Omega} = 1.126 \times 10^{-26} \text{ cm}^2$, was obtained from [34]. The density of scatterers was calculated from the ideal gas law, $n_{gas} = \frac{p_{gas}}{k_B T_{gas}}$, where k_B is the Boltzmann constant, p_{gas} is the gas pressure, and $T_{gas} = 298 \text{ K}$ is the gas temperature. Thus, the RS signal can be written as

$$S_{RS} = \alpha \bar{E}_L^{RS} p_{gas}, \quad \alpha = \frac{\lambda_L}{hc} \frac{1}{A_L} \frac{d\sigma_{RS}}{d\Omega} \frac{1}{k_B T_{gas}} V \Omega K, \quad (15)$$

where α can be obtained from a linear fit to the RS signal as a function of gas pressure and laser energy, as shown in figure B3. It includes most of unknown terms in equation (4) except for the effective lifetime of the excited state, which is discussed in the following section.

Appendix C. Lifetime of the C_2 excited state

The apparent lifetime of the C_2 excited state in an atmospheric pressure plasma strongly depends on the radiation lifetime and quenching rates. Additional terms related to dissociation and coagulation processes leading to the loss of

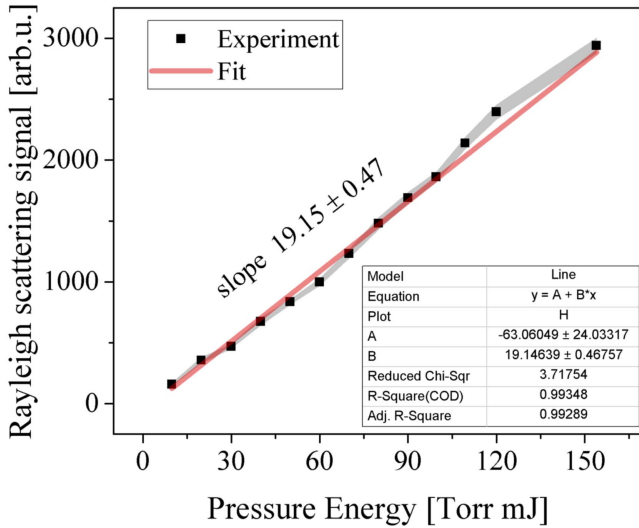


Figure B3. Dependence of the RS signal on product of the gas pressure and laser energy for planar LIF geometry. The gray band represents the measurement errors. The slope α defines the unknown terms in equation (4) used for quantitative planar LIF measurements.

carbon dimers can also shorten the excited state lifetime. The effective lifetime can be written in general form as

$$\tau_{\text{eff}} = \left[A + \sum_i n_i q_i + O \right]^{-1}, \quad (16)$$

where each term is temperature dependent and some terms may depend on the local density of quenchers assuming constant background gas pressure. Here, A is the spontaneous emission coefficient, (corresponding lifetime of 120 ns [35]) and n_i is the quencher number density for quenchers of type i with quenching coefficient q_i . The last term, O , represents all other processes leading to reduction of the lifetime of the state. When quenching rates are known for certain quenchers in gas mixtures, their dependence on temperature and number density complicates the use of equation (16) in most cases when non-stationary atmospheric plasma is involved as is the case for the carbon arc [26, 27].

The first measurements of the LIF signal decay revealed that the effective lifetime of the excited state is comparable to the laser pulse duration, 8 ns, as shown in figure C1. However, after the extinction of the laser pulse, the rate equation for the excited state is reduced to a decay problem with a single-exponential solution characterized by the effective life time τ_{eff} :

$$\frac{dn_{\text{exc}}}{dt} = -\frac{n_{\text{exc}}}{\tau_{\text{eff}}}, \quad (17)$$

where n_{exc} is the population of the excited state.

Therefore, the decay time of the LIF signal was measured starting 10 ns after the extinction of the laser pulse beginning with the lower background gas pressure for which the decay time is longer. The pressure was gradually increased to 500 Torr keeping all other parameters identical, e.g. discharge current and voltage, PMT bias voltage, laser beam energy, etc. Since the helium is a viscous medium preventing expansion of the arc plasma, the pressure decrease led to expansion of the C_2 bubble. Thus, the detection window was scanned to find the maximum

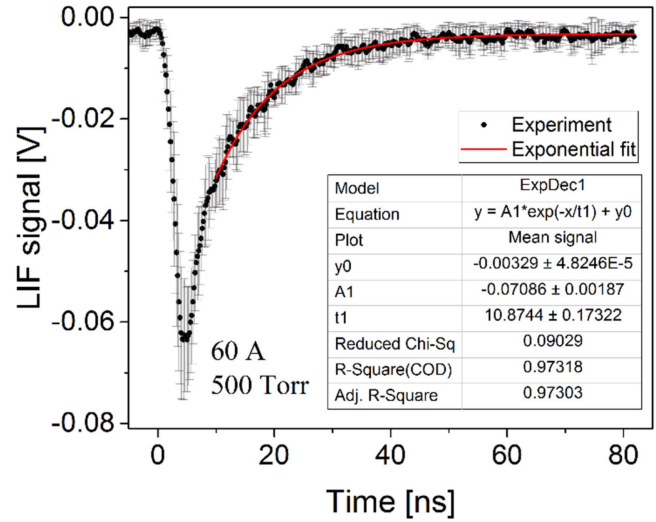


Figure C1. The measured LIF signal decay.

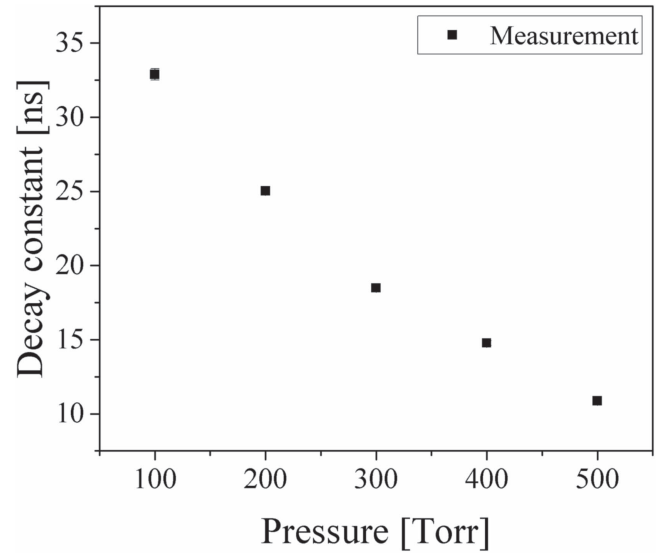


Figure C2. Effective lifetime of the excited state of C_2 as a function of background gas pressure.

C_2 density at each pressure value and the corresponding decay time was measured. The obtained pressure dependence of the decay time is shown in figure C2.

Appendix D. Saturation effect

Compared with conventional LIF, the planar LIF geometry makes possible instantaneous measurements of fluorescence over a large area with high spatial and temporal resolution. This is valuable for measurements in the arc discharge for nanomaterial synthesis, which is characterized by fast shape variation and unpredictable motion [26, 27]. However, this implies a strong requirement for single shot measurements by planar LIF. Since spontaneous emission is the main contributor to the background level in the planar LIF measurements, the choice of C_2 excitation scheme (3, 1) was the one

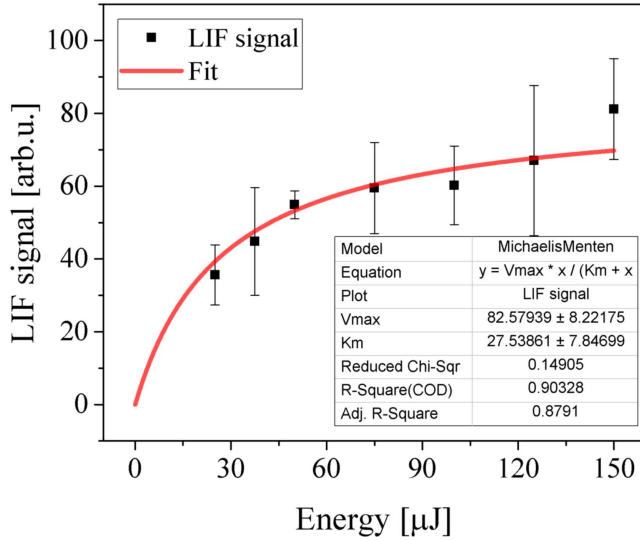


Figure D1. Saturation curve for the planar LIF diagnostic. The fit provides the saturation parameter s . The last point of the experimental curve was excluded from the fit.

with the largest SNR ratio. Transitions with low vibrational quantum numbers such as, (0, 0), (0, 1), etc, are more intense, meaning that their upper states are well populated and thus effect of the population increase due to stimulated absorption of laser photons may not be large.

Another option is to increase the laser energy since the LIF signal is proportional to the laser energy. This applies until the contribution of laser-stimulated emission is small and does not affect the population of the excited state. In general, this effect of transition saturation can be accounted for by the saturation parameter s , which affects the LIF signal according to:

$$S_{\text{LIF}} = Y_{\text{LIF}} \frac{E_L}{1 + sE_L}, \quad (18)$$

where E_L is the laser energy, S_{LIF} is the measured LIF signal and Y_{LIF} is the LIF signal per unit laser energy without the saturation effect. For the planar LIF geometry the saturation parameter becomes a function of transversal beam coordinate following the spatial profile of the laser intensity shown in figure B2. However, it was impossible to derive such a dependence due to large error bars. Therefore, the saturation parameter was calculated from the fit of the calibration curve shown in figure D1 with integrated LIF signal. The measured LIF signal was then corrected using the obtained parameter $s = 0.036 \pm 0.01$ ($1 \mu\text{J}^{-1}$) and $Y_{\text{LIF}} = 3.00 \pm 1.15$ ($1 \mu\text{J}^{-1}$).

Appendix E. Mixture composition calculations

We performed computations of the C–He mixture composition based on our experimental conditions using the same approach as in [20]—minimization of the Gibbs energy. The results are shown in figure E1.

The ratio of the C_2 concentration to the total concentration of carbon, C_{total} , is calculated for different compositions of He–C mixture (shown in the legend bars, 0.01, 0.1, and 1).

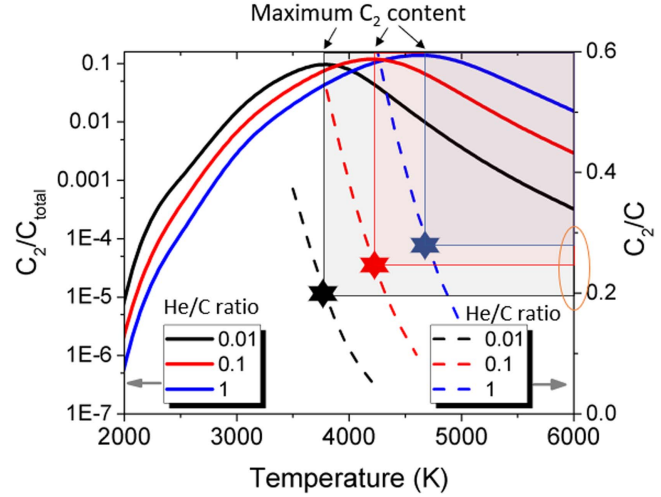


Figure E1. Calculated ratio of $\text{C}_2/\text{C}_{\text{total}}$ and C_2/C for different composition of He/C shown in legend bars. For the maximum concentration of C_2 , the ratio C_2/C is within a narrow range (0.2;0.3).

Similarly, the ratios of C_2 to C (carbon atoms) are calculated (dashed lines in figure E1) but near the maximum content of the C_2 in the He–C mixture. The obtained ratio C_2/C is within a narrow range of (0.2;0.3) and can be safely assumed to be 0.25 for a wide range of He–C mixture compositions.

Appendix F. Ex situ evaluation of low ablation products

The differences in C_2 observed during high and low ablation mode correlate to the carbon nanomaterials produced in volume during each mode, respectively. Low ablation mode is presented below while characterization of comparable materials grown in high ablation mode can be found in our previous work Yatom *et al* [30]. While both modes produce SWCNTs, SWCNHs, and amorphous carbon, the ratio of SWCNTs to other carbon nanomaterials is higher for samples collected in high ablation mode than low ablation mode.

Samples of CNTs produced in the low ablation mode were collected on copper wires that had been placed near the anode during arc operation. Nanomaterials were analyzed using Raman spectroscopy and TEM. The material collected on the wires was analyzed directly using a Horiba LabRam ARAMIS Raman spectrometer at 532 nm (2.33 eV) and 633 nm (1.96 eV). Figure F1(a) shows the full Raman spectra of these nanomaterials at 532 nm with all characteristic modes for CNTs: radial breathing mode (RBM), D, G–, G+, M–, M+, iTOLA, G', 2LO, and 2G [36]. The relatively high ratio of D to G–/G+ is indicative of the presence of SWCNHs [37]. A broad feature at $\sim 1535 \text{ cm}^{-1}$ is attributable to amorphous carbon [38]. The presence of RBMs with both 532 and 633 nm excitation (figure F1(b)) confirms the presence of SWCNTs with a range of diameters [36].

TEM grids were the prepared of the materials analyzed by Raman using dry transfer. These samples were surveyed using a FEI Talos F200X scanning/TEM. The nanomaterials

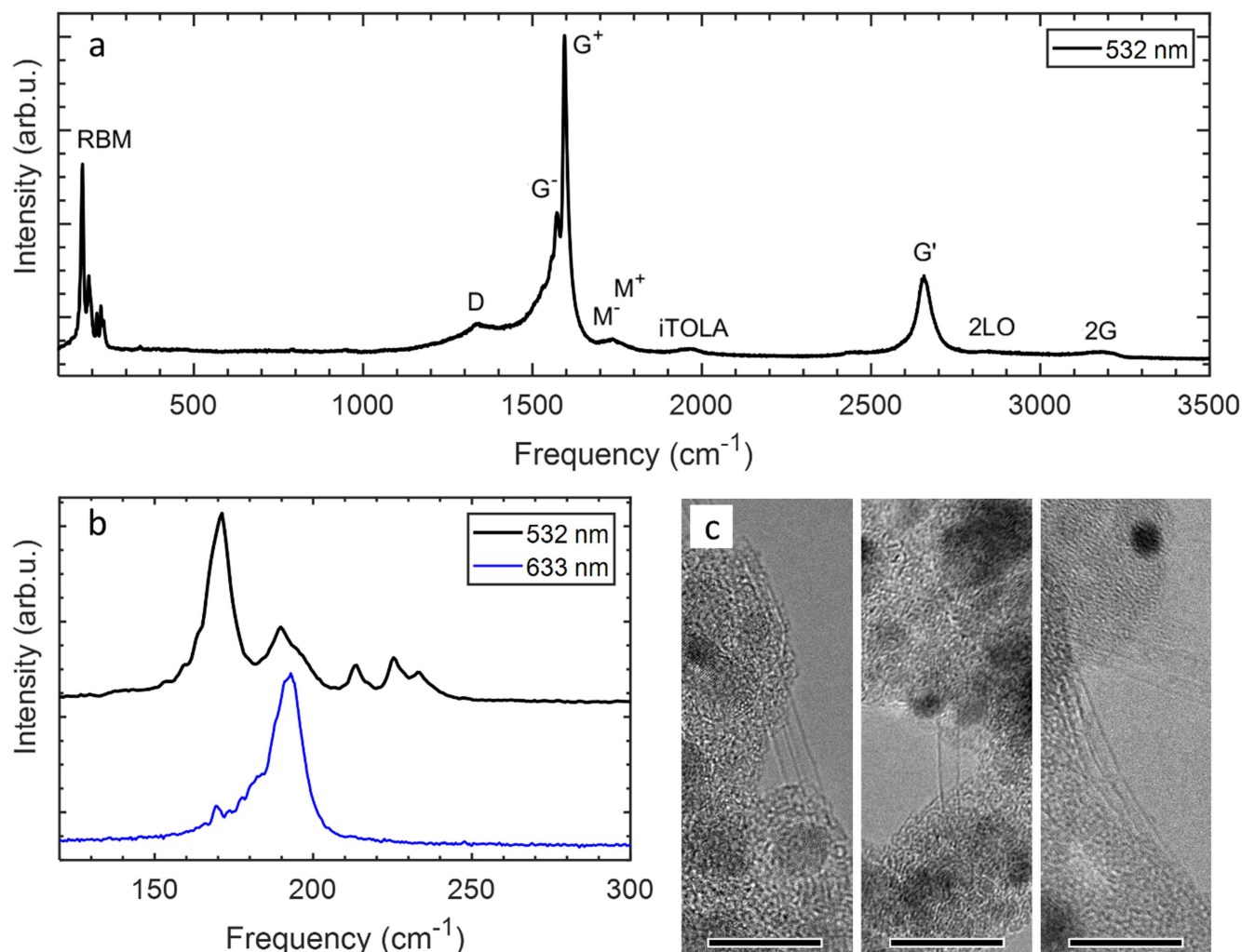


Figure F1. Raman spectra of nanomaterials produced in low ablation mode. (a) Spectra obtained of as-synthesized nanomaterials with the characteristic vibrational peaks labeled. (b) Expanded view of low frequency Raman bands showing the RBM features characteristic of SWCNTs. (c) TEM images showing SWCNTs, SWCNHs, metallic particles (all scale bars 10 nm).

were observed to be predominantly SWCNHs and metal nanoparticles. CNTs were a small fraction of the total nanomaterials imaged. Only SWCNTs (no double or multiwalled nanotubes) were observed (figure F1(c)).

ORCID iDs

V Vekselman <https://orcid.org/0000-0002-8071-1990>
 A Khrabry <https://orcid.org/0000-0002-2855-7148>
 I Kaganovich <https://orcid.org/0000-0003-0653-5682>
 B Stratton <https://orcid.org/0000-0001-8830-3003>
 R S Selinsky <https://orcid.org/0000-0002-4874-5947>
 Y Raites <https://orcid.org/0000-0002-9382-9963>

References

- [1] Fang X Q, Shashurin A, Teel G and Keidar M 2016 Determining synthesis region of the single wall carbon nanotubes in arc plasma volume *Carbon* **107** 273–80
- [2] Journet C, Maser W K, Bernier P, Loiseau A, delaChapelle M L, Lefrant S, Deniard P, Lee R and Fischer J E 1997 Large-scale production of single-walled carbon nanotubes by the electric-arc technique *Nature* **388** 756–8
- [3] Iijima S and Ichihashi T 1993 Single-shell carbon nanotubes of 1 nm diameter *Nature* **363** 603–5
- [4] Volotskova O, Levchenko I, Shashurin A, Raites Y, Ostrikov K and Keidar M 2010 Single-step synthesis and magnetic separation of graphene and carbon nanotubes in arc discharge plasmas *Nanoscale* **2** 2281–5
- [5] Iijima S 1991 Helical microtubules of graphitic carbon *Nature* **354** 56–8
- [6] Journet C, Picher M and Jourdain V 2012 Carbon nanotube synthesis: from large-scale production to atom-by-atom growth *Nanotechnology* **23** 142001
- [7] Arora N and Sharma N N 2014 Arc discharge synthesis of carbon nanotubes: comprehensive review *Diam. Relat. Mater.* **50** 135–50
- [8] Meyyappan M 2011 Plasma nanotechnology: past, present and future *J. Phys. D: Appl. Phys.* **44** 174002
- [9] Lange H 1997 Spectral diagnostics of helium-carbon arc plasma during carbon nanostructure formation *Fullerene Sci. Technol.* **5** 1177–201

- [10] Huczko A, Lange H, Byszewski P, Koshio A and Shinohara H 1999 Carbon arc plasma doped with Fe and Co/Ni: spectroscopy and formation of carbon nanostructures *Electronic Properties of Novel Materials—Science and Technology of Molecular Nanostructures* vol 486, pp 258–62
- [11] Lange H, Huczko A, Sioda M and Louchev O 2003 Carbon arc plasma as a source of nanotubes: emission spectroscopy and formation mechanism *J. Nanosci. Nanotechnol.* **3** 51–62
- [12] Lange H, Labedz O, Huczko A and Bystrzejewski M 2011 Emission and absorption spectroscopy of carbon arc plasma during formation of carbon magnetic encapsulates *Dusty/Complex Plasmas: Basic and Interdisciplinary Research* vol 1397
- [13] Akita S, Ashihara H and Nakayama Y 2000 Optical emission spectroscopy of arc flame plasma for generation of carbon nanotubes *Japan. J. Appl. Phys.* **39** 4939–44
- [14] Nishio M, Akita S and Nakayama Y 2004 Effect on the growth of carbon nanotubes and optical emission spectroscopy in short-period arc-discharge *Thin Solid Films* **464** 304–7
- [15] Cau M, Dorval N, Attal-Tretout B, Cochon J L, Foutel-Richard A, Loiseau A, Kruger V, Tsurikov M and Scott C D 2010 Formation of carbon nanotubes: *in situ* optical analysis using laser-induced incandescence and laser-induced fluorescence *Phys. Rev. B* **81** 165416
- [16] Cau M, Dorval N, Cao B, Attal-Tretout B, Cochon J L, Loiseau A, Farhat S and Scott C D 2006 Spatial evolutions of Co and Ni atoms during single-walled carbon nanotubes formation: measurements and modeling *J. Nanosci. Nanotechnol.* **6** 1298–308
- [17] Dorval N *et al* 2004 *In situ* optical analysis of the gas phase during the formation of carbon nanotubes *J. Nanosci. Nanotechnol.* **4** 450–62
- [18] Pierson H O 1993 *Handbook of Carbon, Graphite, Diamond and Fullerenes* (Park Ridge, NJ: Noyes Publications)
- [19] Yatom S, Bak J, Khrabryi A and Raites Y 2017 Detection of nanoparticles in carbon arc discharge with laser-induced incandescence *Carbon* **117** 154–62
- [20] Wang W Z, Rong M Z, Murphy A B, Wu Y, Spencer J W, Yan J D and Fang M T C 2011 Thermophysical properties of carbon–argon and carbon–helium plasmas *J. Phys. D: Appl. Phys.* **44** 355207
- [21] Wang Q, Ng M F, Yang S W, Yang Y H and Chen Y A 2010 The mechanism of single-walled carbon nanotube growth and chirality selection induced by carbon atom and dimer addition *ACS Nano* **4** 939–46
- [22] Gómez-Gualdrón D A, Beetge J M, Burgos J C and Balbuena P B 2013 Effects of precursor type on the CVD growth of single-walled carbon nanotubes *J. Phys. Chem. C* **117** 10397–409
- [23] Amorim J, Baravian G and Jolly J 2000 Laser-induced resonance fluorescence as a diagnostic technique in non-thermal equilibrium plasmas *J. Phys. D: Appl. Phys.* **33** R51–65
- [24] Vekselman V, Gleizer J, Yatom S, Yarmolich D, Gurovich V T, Bazalitski G, Krasik Y E and Bernshtam V 2009 Laser induced fluorescence of the ferroelectric plasma source assisted hollow anode discharge *Phys. Plasmas* **16** 113504
- [25] McMillin B K, Biswas P and Zachariah M R 2011 *In situ* characterization of vapor phase growth of iron oxide-silica nanocomposites: I. 2D planar laser-induced fluorescence and Mie imaging *J. Mater. Res.* **11** 1552–61
- [26] Vekselman V, Feurer M, Huang T, Stratton B and Raites Y 2017 Complex structure of the carbon arc discharge for synthesis of nanotubes *Plasma Sources Sci. Technol.* **26** 065019
- [27] Gershman S and Raites Y 2016 Unstable behavior of anodic arc discharge for synthesis of nanomaterials *J. Phys. D: Appl. Phys.* **49** 345201
- [28] Ng J and Raites Y 2015 Self-organisation processes in the carbon arc for nanosynthesis *J. Appl. Phys.* **117** 063303
- [29] Levchenko I, Keidar M, Xu S Y, Kersten H and Ostrikov K 2013 Low-temperature plasmas in carbon nanostructure synthesis *J. Vac. Sci. Technol. B* **31** 050801
- [30] Yatom S, Selinsky R S, Koel B E and Raites Y 2017 ‘Synthesis-on’ and ‘synthesis-off’ modes of carbon arc operation during synthesis of carbon nanotubes *Carbon* **125** 336–43
- [31] Almeida N A, Benilov M S and Naidis G V 2008 Unified modelling of near-cathode plasma layers in high-pressure arc discharges *J. Phys. D: Appl. Phys.* **41** 245201
- [32] Khrabry A, Kaganovich I, Nemchinsky V and Khodak A 2018 Investigation of a short argon arc with hot anode: I. Numerical simulations of non-equilibrium effects in the near-electrode regions *Phys. Plasmas* **25** 013521
- [33] Bird B R, Stewart W E and Lightfoot E N 1960 *Transport Phenomena* (New York: Wiley)
- [34] Miles R B, Lempert W R and Forkey J N 2001 Laser Rayleigh scattering *Meas. Sci. Technol.* **12** R33–51
- [35] Tatarczyk T, Fink E H and Becker K H 1976 Lifetime measurements on single vibrational levels of C-2(D3iig) by laser fluorescence excitation *Chem. Phys. Lett.* **40** 126–30
- [36] Dresselhaus M S, Dresselhaus G, Saito R and Jorio A 2005 Raman spectroscopy of carbon nanotubes *Phys. Rep.* **409** 47–99
- [37] Pena-Alvarez M, del Corro E, Langa F, Baonza V G and Taravillo M 2016 Morphological changes in carbon nanohorns under stress: a combined Raman spectroscopy and TEM study *RSC Adv.* **6** 49543–50
- [38] Ferrari A C and Robertson J 2004 Raman spectroscopy of amorphous, nanostructured, diamond-like carbon, and nanodiamond *Phil. Trans. R. Soc. A* **362** 2477–512